THE JOURNAL OF PHYSICAL CHEMISTRY C

Article

pubs.acs.org/JPCC

Synergistic Behavior of Tubes, Junctions, and Sheets Imparts Mechano-Mutable Functionality in 3D Porous Boron Nitride Nanostructures

Navid Sakhavand[†] and Rouzbeh Shahsavari*[,†,‡,§]

[†]Department of Civil and Environmental Engineering, [‡]Department of Material Science and NanoEngineering, and [§]Smalley Institute for Nanoscale Science and Technology, Rice University, Houston, Texas 77005, United States

Supporting Information

ABSTRACT: One-dimensional (1D) boron nitride nanotube (BNNT) and 2D hexagonal BN (*h*-BN) are attractive for demonstrating fundamental physics and promising applications in nano-/microscale devices. However, there is a high anisotropy associated with these BN allotropes as their excellent properties are either along the tube axis or in-plane directions, posing an obstacle in their widespread use in technological and industrial applications. Herein, we report a series of 3D BN prototypes, namely, pillared boron nitride (PBN), by fusing single-wall BNNT and monolayer *h*-BN aimed at filling this gap. We use density functional theory and molecular dynamics simulations to probe the diverse mechano-mutable properties of PBN prototypes. Our results demonstrate that the synergistic effect of the tubes, junctions, and sheets imparts cooperative deformation mechanisms, which overcome the intrinsic limitations of the PBN constituents and provide a number of superior characteristics including 3D balance of strength and toughness, emergence of negative Poisson's ratio, and elimination of strain softening along the armchair orientation. These features, combined with the ultrahigh surface area and lightweight structure, render PBN as a 3D multifunctional template for applications in graphene-based nanoelectronics, optoelectronics, gas storage, and functional composites with fascinating in-plane and out-of-plane tailorable properties.

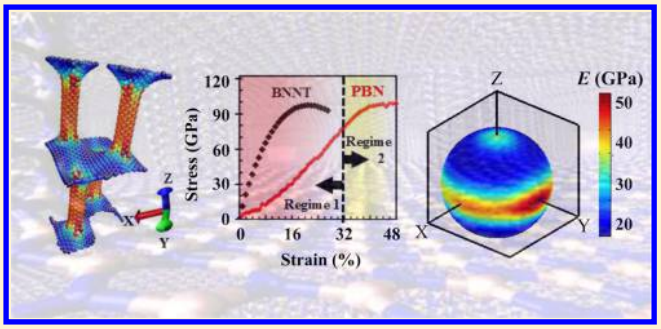

1. INTRODUCTION

Boron nitride (BN) is a wide band gap III−V compound consisting of equal proportions of B and N atoms.[1,2] The BN nanotube (BNNT) and hexagonal BN (*h*-BN) are comprised of alternating B and N atoms in a honeycomb arrangement similar to carbon nanotubes[3] (CNTs) and graphene[4] structures, respectively. Manifestation of a quantum-confinement effect in these low-dimensional structures provides them with superb material properties. While thermal conductivity[5] and mechanical stability[6] of these one-dimensional (1D) and two-dimensional (2D) BN morphologies are comparable to CNT and graphene, their electrically insulating properties,[7] high temperature resistance,[2,8] piezoelectricity,[9] and distinguishable chemical inertness[8] make them distinct from their carbonaceous analogues. Among key specifications of these BN nanostructures are their highly anisotropic properties. Whereas *h*-BN exhibits excellent in-plane mechanical strength and thermal conductivity, the out-of-plane strength and thermal coupling are limited by weak van der Waals (vdW) interactions and could become a mechanical weakness and thermal dissipation bottleneck. Similarly, BNNT shows great properties along the tube axis (e.g., yield strength comparable to CNTs[10] and thermal conductivity of ~350 W/m-K).[11]

Over the past few years, efforts have been made to fabricate several hybrid nanomaterials with modified or novel properties that typically are more attractive than their individual constituents. In the context of hybrid, low-dimensional materials, the majority of the research has been focused on carbon-based structures. Examples include carbon nanopeapod,[12] carbon nanobuds,[13] periodic graphene nanobuds,[14] pillared graphene,[15] and so on. The hybrid forms of BN are mainly fabricated in the group of ternary BCN materials by doping B and N in carbon systems or vice versa.[16] Examples comprise BCN-based nanotubes[17,18] and BCN-based nanostructures.[19] Other classes of hybrid BCN materials are obtained via direct deposition of *h*-BN on graphene,[20] or direct growth of graphene on *h*-BN,[21] or artificially stacked graphene-BN van der Waals solids.[22] Both theoretical and experimental studies suggest that hybrid nanomaterials can leverage the best aspects of their constituents and/or render new functionalities depending on the structural integrity and interfacial chemical bonding of the constituents.[14,16] However, in spite of the promising future of BNNT and *h*-BN, to our knowledge, there are no reported hybrid BN structures that encompass various BN allotropes to render enhanced or new properties—especially when compared to CNTs and gra-

Received: May 6, 2014
Revised: July 14, 2014
Published: July 14, 2014

   dx.doi.org/10.1021/jp5044706 | J. Phys. Chem. C 2014, 118, 22730−22738

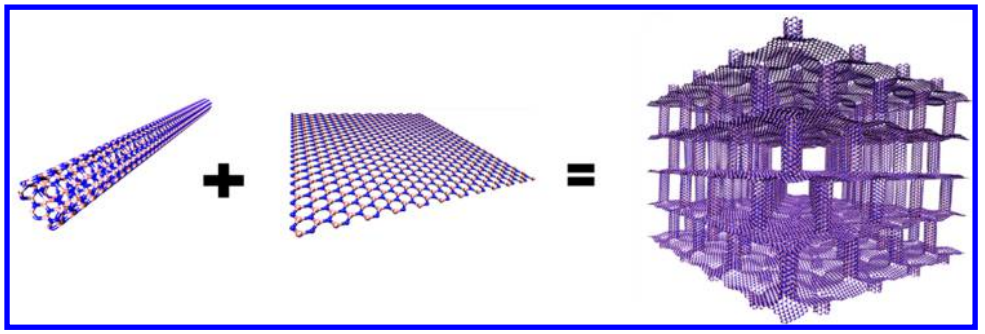

Figure 1. Schematic picture of PBN made of 1D BNNT and 2D monolayer *h*-BN sheets.

phene.[23] In this study, we report a new series of hybrid BN nanostructures by fusing single-wall BNNT and monolayer *h*-BN allotropes to create pillared boron nitride (PBN), which imparts several 3D mechano-mutable properties.

2. COMPUTATIONAL METHODS

2.1. Molecular Dynamics Methods. The LAMMPS package[24] was used for MD simulations. A bond-order Tersoff-like potential parametrized for BN[25] is adopted to account for the interatomic interactions. This force field has proved to present characteristics of both BN sheets and BN nanotubes in previous studies.[26−29] To validate the accuracy of the force field potential in our simulations, the stress−strain plot of a (6,6) BNNT obtained from the MD simulations was compared with the results of our density functional theory (DFT) calculations on a (6,6) BNNT with 148 atoms (Figure S1, Supporting Information). It is observed that the MD simulations closely match with our DFT results, thus confirming the accuracy of the force field potential. Before calculating mechanical properties, each PBN prototype was relaxed for 1 ns under the isothermal−isobaric ensemble (NPT) at zero pressure and temperature with the Nose−Hoover thermostat[30,31] for the time integration. All MD simulations were performed with a time step of 1 fs. All the mechanical (elastic and inelastic) properties were obtained by energy minimization at 0 K to exclude thermal effects. All visualizations have been carried out using the Visual Molecular Dynamics (VMD) virtualization package,[32] and stress counters were created by Atomeye, an atomistic configuration viewer package.[33]

2.1.1. Calculation of Elastic Properties. Prior to calculating the elastic properties, we perform energy minimizations by the conjugate gradient method as implemented in LAMMPS to fully relax the PBN prototypes. Next, we adopted the stress−strain approach[14] to apply six strains to the cell coordinates to calculate the full elastic constant tensors. For each strain, we relaxed the system while the box dimensions were fixed. Then, by calculating the stress tensor via the virial theorem[34] we constructed a linear system relating stresses to strains by generalized Hooke's law in linear elasticity

$$\begin{bmatrix}\sigma_1\\ \sigma_2\\ \sigma_3\\ \sigma_4\\ \sigma_5\\ \sigma_6\end{bmatrix} = \begin{bmatrix} C_{11} & C_{12} & C_{13} & C_{14} & C_{15} & C_{16}\\ C_{12} & C_{22} & C_{23} & C_{24} & C_{25} & C_{26}\\ C_{13} & C_{23} & C_{33} & C_{34} & C_{35} & C_{36}\\ & & & C_{44} & C_{45} & C_{46}\\ & & & & C_{55} & C_{56}\\ \text{Sym} & & & & & C_{66}\end{bmatrix} \begin{bmatrix}\epsilon_1\\ \epsilon_2\\ \epsilon_3\\ \epsilon_4\\ \epsilon_5\\ \epsilon_6\end{bmatrix} \quad (1)$$

In the above, σ and ε represent the stress and strain, while C_{ij} denotes the elastic constant components shown in contracted Voigt notation. By applying any nonzero strain in eq 1 and calculating stresses, one can calculate a column of elastic constants. Thus, by repeating this procedure for all six strains we cover the whole elastic tensor. In this approach, off-diagonal components appear twice in the calculations, and to have a better estimate we take the average of the two equivalent off-diagonal terms. Hence, by using an orthogonal matrix factorization and the best least-squares fit, elastic constants can be found by minimizing[35]

$$|(\sigma_i - \sigma_r) - C_{ij}(\varepsilon_i - \varepsilon_r)| \quad (2)$$

Here σ_r and ε_r are residual stress and residual strain; $(\varepsilon_i - \varepsilon_r)$ is the applied strain; and the repeated indices indicate the Einstein summation rule. In this method, the uncertainty in C_{ij} values will be minimized with enhanced overall accuracy. This method has been successfully used to predict elastic constants of several crystalline materials.[35] We applied 5% strain in all six directions to calculate the elastic constants.

Once an elastic tensor, **C**, is obtained, we inverted it to get the compliance tensor, $\mathbf{S} = C^{-1}$. Then, the Young moduli along different orthogonal directions are[36]

$$E_1 = \frac{1}{S_{11}}, \quad E_2 = \frac{1}{S_{22}}, \quad E_3 = \frac{1}{S_{33}} \quad (3a,b,c)$$

In eq 3, S_{11} refers to the first component of the compliance tensor and so on, and the indices 11, 22, and 33 denote respectively, *X*, *Y*, and *Z* directions. Then, the 3D elastic Young moduli along any arbitrary direction in space are calculated via classical rotation of a compliance matrix.[36] The anisotropic Poisson's ratios can also be obtained from the compliance tensor via

$$\nu_{ij} = -\frac{S_{ij}}{S_{ii}} \quad i, j = 1, 2, 3 \text{ and } i \neq j \quad (4)$$

2.1.2. Calculation of Inelastic Properties. The inelastic properties (stress−strain plots) in each direction were obtained by applying strains at the increments of 1% in the corresponding direction while restraining the system against displacement in the other directions. The system was then allowed to relax, and the stress tensor was obtained via the virial theorem.[34] Stress−strain calculations were also repeated with 0.1% strain increments, which did not show a noticeable difference with the results from 1% strain increments.

2.2. Density Functional Theory (DFT) Calculations. To optimize the conformation of the junction, we used density functional theory (DFT)[37] based on Becke's three-parameter hybrid functional combined with the Lee−Yang−Parr correlation functional (B3LYP) with the 6-31+G* basis set. These calculations were performed using the Gaussian 09 suite

dx.doi.org/10.1021/jp5044706 | J. Phys. Chem. C 2014, 118, 22730−22738

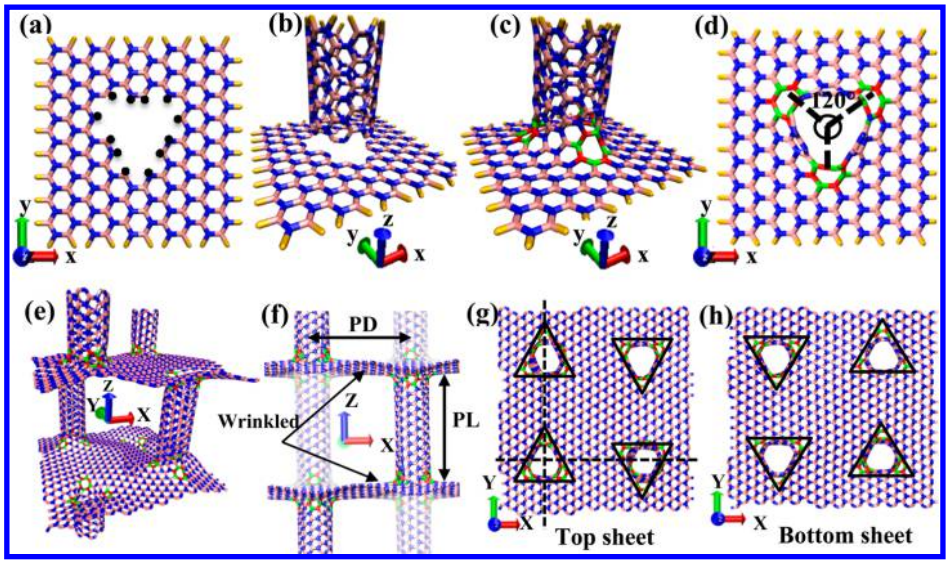

Figure 2. Procedure of constructing PBN. (a) The geometry of a defected *h*-BN monolayer sheet. The black dots represent the joined positions that lack a bond to satisfy sp^2 configuration. (b) A (6, 6) BNNT and a defected *h*-BN ready to form the junction. (c) The system is fully optimized with DFT calculation and satisfies Euler's theorem. (d) A top view of the junction. (e) Schematic view of a typical unit cell of PBN, which includes four columns and two sheets. (f) A side view of PBN. Due to asymmetric junctions, BN sheets tend to be wrinkled. Pillar length (PL) represents the average height of the BN nanotubes. Interpillar distance (PD) denotes the average distance between the centers of the BN nanotubes. PDs along *X* and *Y* axes are identical. Note that the nanotubes are discontinued at the junctions with the sheets; nanotubes located farther on the *Y* axes are faded in color. (g) to (h) show the cross-section of PBN viewed along the *Z* axis at the intersection of the tubes and the sheets. The vertices of the black triangles represent the location of octagon rings at the junctions. In (a) to (h) B atoms are in pink, and N atoms are in blue. In the octagon rings, the B and N atoms are shown in red and green, respectively. At nonperiodic edges, hydrogen atoms (shown in yellow) fulfill sp^2 configuration.

of programs.[38] To validate the accuracy of the used force-field potential, we obtained the stress−strain plot of BNNT along its tube axis by performing DFT calculations on a (6,6) BNNT with 148 atoms (72 B and 72 N). We employed the GGA exchange correlation functional with ultrasoft pseudopotentials[39] with a plane-wave basis set and a cutoff energy of 420 eV for the wave functions and 5035 eV for the charge density, as implemented in the PWSCF package of Quantum Espresso distribution.[40] We used periodic boundary conditions along the axis tube. The size of the vacuum in the in-plane direction was 16 Å. Before calculating the stress−strain plot, we performed energy minimizations to fully relax the system. Then, we applied incremental strains of 1% in the tube axis, and after each strain the box size was fixed. Then, the system was relaxed until each of the *X*, *Y*, and *Z* components of the force on any single atom was below 0.01 eV/Å. As the system size was large (148 atoms), we used γ-point sampling of the Brillouin zone. Figure S1 (Supporting Information) shows the stress−strain plot of BNNT obtained from the DFT calculations, which validates the MD predictions.

3. RESULTS AND DISCUSSIONS

3.1. Construction of PBN Prototypes. *3.1.1. Creation of the Junction.* Figure 1 shows a general schematic picture of 3D PBN made of 1D BNNT and 2D monolayer *h*-BN sheets. A key attribute of the PBN is the junction between the tubes and sheets for which there are several possibilities depending on the tube radius and chirality.[41] However, all possible configurations should satisfy Euler's theorem of polygons,[42] which allows determining the bond surplus, i.e., the excess in the number of polygonal sites compared with the normal value for the junction.[12] Unlike hybrid carbon-based materials, in the case of hybrid BN structures with alternating B and N atoms and sp^2 configuration, only rings with an even number of sides (e.g., hexagons, octagons, etc.) are energetically favorable at the junctions. In other words, the proximity of two B (or two N) atoms is not energetically favorable. This relates the number of distinct defects to the so-called necklace and bracelet problems of combinatorial theory where the relation $E = 6 + 2J$ should hold for each defect.[43] Here, *E* is the number of edges, and *J* is the number of joining positions (the black dots in Figure 2a). We chose a defect configuration as shown in Figure 2a ($E = 30$, $J = 12$) for which only an armchair BNNT can satisfy the Euler's theorem.[43] According to this theorem, the number of faces, *F*, vertices, *V*, edges, *E*, and genus, *G*, obey $F + V = E + 2 - 2G$.[12] The BNNT and BN sheet can be mapped into a closed surface of genus 2, which means that a bond surplus of 12 should be shared between the BNNT and sheet (6 per each). For the BN structure, BN hexagon and octagon have a bond surplus of 0 and +2, respectively.

In our study, the junction was created computationally by bringing a (6,6) single-wall BNNT close to a defected *h*-BN monolayer sheet to form a 3D building block (Figure 2a,b). The specific form of the defect in *h*-BN, shown in Figure 2a, is consistent with the (6,6) BNNT to satisfy the sp^2 configuration for all the atoms at the junction.[43] We fused the nanotube and the sheet in Figure 2b by fully optimizing the system with DFT calculations to create the basic 3D building block (Figure 2c). The final structure of the junction has three octagons, while the rest are all hexagons, in agreement with Euler's rule. Interestingly, the odd number of the octagon rings in this particular arrangement imposes the junction to form a triangular-type shape (Figure 2d).

3.1.2. PBN Unit Cell with Periodic Boundary Conditions. The 3D building block in Figure 2c was extended to 3D pillared motifs using a series of transformations and rotations to create the 3D unit cell of PBN with periodic boundary conditions. The final structure and cell dimensions are obtained by relaxing

dx.doi.org/10.1021/jp5044706 | J. Phys. Chem. C 2014, 118, 22730−22738

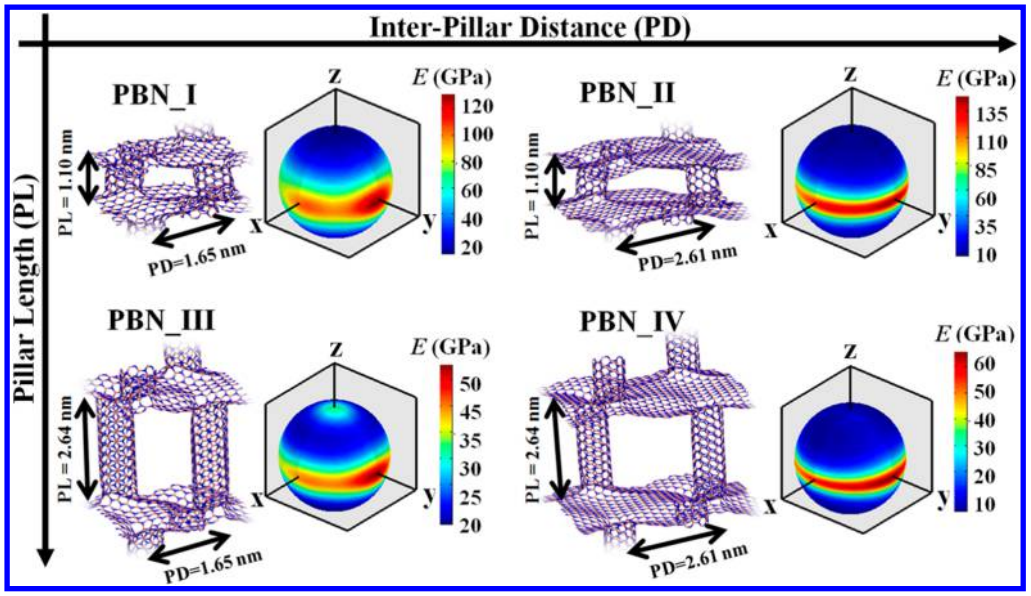

Figure 3. Atomistic view of PBN_I to IV prototypes and their 3D contour of elastic moduli along any arbitrary direction in space. Any point on the sphere with the unit radius represents the tip of a unit vector, which is drawn from the center of the sphere (intersection of the three PBN planes). The surface of the sphere covers all possible 3D arbitrary unit vectors. PBN prototypes in the same columns (rows) have identical PDs (PLs). The *XY*, *XZ*, and *YZ* planes intersecting the spheres represent the planes of PBN prototypes and are not drawn in scale.

Table 1. Number of Atoms, Structural Details, and Surface Areas of Four PBN Prototypes

				unit cell size (nm)				
PBN prototype	number of atoms	pillar length, PL (nm)	pillar distance, PD (nm)	Lx	Ly	Lz	surface area/mass (m^2/g)	density (kg/m^3)
PBN_I	1088	1.10	1.65	3.40	3.46	2.54	2467.05	750.28
PBN_II	2112	1.10	2.61	5.17	4.99	2.69	2274.37	627.09
PBN_III	1760	2.64	1.65	3.40	3.46	6.09	2547.31	506.20
PBN_IV	2784	2.64	2.61	5.17	4.99	6.28	2378.90	354.08

the unit cell via MD simulation under an isothermal−isobaric ensemble. Figure 2e,f represents a typical PBN unit cell, which includes four columns joining two parallel planes of *h*-BN sheets. At each junction, the octagon rings are located at the vertices of a somewhat triangular-shape defect (Figure 2g,h). Thus, each junction is locally symmetric along the *Y* axis (zigzag) but asymmetric along the *X* axis (armchair). After MD relaxation of the unit cell, such specific junction alignment causes the BN sheets to be wrinkled in both *X* and *Y* directions (Figure 2f). Therefore, even in the absence of external force, both the junctions and the BN sheets are slightly stressed due to the imposed curvature. Such wrinkles have not been observed in analogous 3D carbon structures, which have an even number of nonhexagonal rings symmetrically aligned in the armchair and zigzag orientations.[15]

Besides junctions, the interpillar distance (PD) and pillar length (PL) are two important structural parameters that define PBN properties (Figure 2f). To reveal the effect of these parameters and explore their cooperation with the junctions, we consider two different PDs and PLs and create four distinct PBN prototypes, namely, PBN_I to PBN_IV (Figure 3). The number of atoms and structural details of these four PBN prototypes are in Table 1.

3.2. Elastic Properties of PBN Prototypes. Equations S1−S4 (Supporting Information) show the calculated elastic constant tensors (stiffness matrices) of PBN_I to PBN_IV in GPa. While the elastic tensors are suggestive of an anisotropic behavior, the extent of this anisotropy differs from PBN_I to IV. To better understand this, we calculated the variation of Young's moduli along any arbitrary direction in space via rotation of elastic stiffness tensors.[36] Figure 3 shows the data in the form of 3D contours of elastic moduli, which upon linking with the PBN structures provide important physical insights to be discussed next.

First, from the 3D contours, it appears that there is a distinct behavior along the in-plane and out-of-plane directions for all PBN prototypes. Indeed, all prototypes represent significant in-plane symmetry, but the extent of the in-plane symmetry varies from PBN_I to PBN_IV. It is observed that structures with larger PDs (PBN_II and PBN_IV) exhibit a more pronounced in-plane symmetry resembling characteristics of transversely isotropic materials. This is because the larger the PDs, the fewer the junctions per unit planar area; thus asymmetric junctions have less influence on breaking the in-plane symmetry.

Second, all PBN prototypes exhibit relatively low stiffness in the out-of-plane direction as compared to the in-plane directions. This can be explained from the discontinuity of the nanotubes, which forces the h-BN sheets to participate in the out-of-plane deformation. However, since h-BNs are known to have low out-of-plane bending stiffness,[23] their contribution results in overall low Young modulus along the out-of-plane direction. However, when the PD is very small, the *h*-BN contributions become minimal, and PBN acts similar to parallel nanotubes. This explains the higher (≈100% and ≈300%) out-of-plane Young moduli of PBN_I and PBN_III than those of PBN_II and PBN_IV, respectively. Similarly, in the planar directions, PBNs with smaller PLs exhibit higher in-plane stiffness owing to the contribution of more nanosheets per unit

dx.doi.org/10.1021/jp5044706 | J. Phys. Chem. C 2014, 118, 22730−22738

area normal to the in-plane direction. This elucidates the higher in-plane Young moduli (≈105% and ≈230%) of PBN_I and PBN_II than those of PBN_III and PBN_IV, respectively. From the above analysis, it appears that the PD/PL ratio is an important characteristic of PBN by which we can control the planar and out-of-plane stiffnesses. We have also studied the effect of PD and PL on orthogonal shear moduli (Figure S2, Supporting Information). It turns out that for all PBN prototypes the in-plane shear modulus, G_{XY}, is higher than out-of-plane shear moduli (G_{XZ} and G_{YZ}) due to the small lateral stiffness of the tubes and flexibility of the junctions.

Note that all the elastic moduli discussed so far are calculated based on a gross (effective) area incorporating large voids in PBN prototypes (Figure 4 and Table 2). Thus, it is not

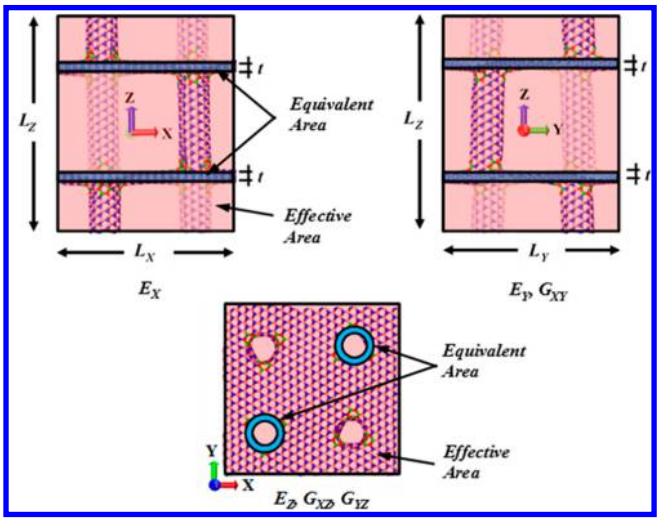

Figure 4. Gross (effective) and equivalent (atomic) areas are shown in red and blue, respectively. The elastic properties associated with each cross-section are shown below the pictures. The symbol t represents the thickness of the nanotubes and nanosheets and is taken to be 0.33 nm.[29]

Table 2. Effective (Gross) and Equivalent (Atomic) Areas for PBN_I to PBN_IV Structures

	effective area (nm^2)					
	Ly.Lz	Lx.Lz	Lx.Ly	Lx.Lz	Lx.Ly	Lx.Ly
PBN_I	8.79	8.64	11.76	8.64	11.76	11.76
PBN_II	13.42	13.91	25.80	13.91	25.80	25.80
PBN_III	21.07	20.71	11.76	20.71	11.76	11.76
PBN_IV	31.34	32.47	25.80	32.47	25.80	25.80
	equivalent area (nm^2)					
	2*Ly.t	2*Lx.t	2πDt	2*Lx.t	2πDt	2πDt
PBN_I	2.35	2.31	1.78	2.31	1.78	1.78
PBN_II	3.39	3.52	1.78	3.52	1.78	1.78
PBN_III	2.35	2.31	1.78	2.31	1.78	1.78
PBN_IV	3.39	3.52	1.78	3.52	1.78	1.78

surprising to get elastic moduli that are 1 or 2 orders of magnitude smaller than those of pure single-wall BNNT and h-BN.[29,44] To get a more realistic comparison between PBN with pure systems, the equivalent moduli of four PBN structures are calculated (Figure S2, Supporting Information). In this case, the net atomic area (equivalent area), as opposed to the gross area, is used to calculate the associated moduli. As a consequence, the elastic moduli are drastically increased with Young's modulus as high as 0.62 TPa in PBN_II and shear modulus of 0.3 TPa in PBN_IV. These values can be readily compared to ≈1 TPa Young's moduli of BNNT[29] and h-BN[44] and ≈0.3 GPa in-plane shear modulus of h-BN.[45]

To present an accurate comparison with other lightweight materials, specific moduli are calculated by dividing the elastic moduli by the apparent density (density including voids) of PBN (apparent density values of different PBN are tabulated in Table 1). The results in Figure S3 (Supporting Information) reveal that specific Young's moduli of PBN (using the effective area) are 80−350 MPa/(kg/m^3). With a similar method, the specific Young's moduli of a single boron nitride tube and boron nitride sheets are calculated to be 435−455 MPa/(kg/m^3). The results show that the 3D PBN exhibits comparable stiffness compared with its 2D substructures, BNNT and h-BN.

To further explore the PBN elasticity, we calculated the in-plane and out-of-plane Poisson's ratios. We found that all PBN prototypes exhibit negative in-plane Poisson's ratios (Table 3)

Table 3. Anisotropic Poisson's Ratios of the Four PBN Prototypes

	vxy	vxz	vyz
PBN_I	−0.2833	0.1519	0.1321
PBN_II	−0.2386	0.0647	0.0586
PBN_III	−0.2669	0.3131	0.2737
PBN_IV	−0.2656	0.1295	0.1255

originating from the curved junctions and wrinkled sheets, which tend to flatten out and exert strains in all lateral directions upon loading (see movies jp5044706_si_002.avi and jp5044706_si_003.avi, Supporting Information). This feature of PBN can be exploited as a design tool to create *auxetic* nanomaterials, i.e., materials that expand (shrink) laterally upon pulling (pushing),[46] with potential applications in sieving, strain sensing, gas separation, and shock energy absorption.[45,46]

3.3. Synergistic Deformation Mechanisms. Mechanical responses beyond elasticity can provide crucial information on deformation mechanisms, which control strength and toughness preceding the materials failure. Using ab initio validated MD simulations, we studied the stress−strain behavior of PBNs along the in-plane and out-of-plane directions until failure. Equivalent areas are used to calculate the stresses to better understand the underlying physics and compare the results with pure systems. Figure 5 shows the results for PBN_IV (as a representative prototype) along with average B−N bond strains and stress contour plots.

3.3.1. Out-of-Plane Deformation. In view of the computational data in Figure 5a, the ultimate strain of PBN ($\varepsilon_U \approx 48\%$) along its out-of-plane direction is ≈80% larger than that of pure BNNT ($\varepsilon_U \approx 27\%$) while maintaining similar ultimate stress, $\sigma_U \approx 100$ GPa. This significant stretching capacity comes from cooperation of two distinct deformation regimes (see movie jp5044706_si_004.avi, Supporting Information). The first regime consists of mainly the out-of-plane deformation of the sheets, i.e., the geometrical rearrangements of the rings in the vicinity of the junctions. In this regime, although tubes are slightly strained, the geometric (rigid body) displacement of the in-plane rings (sheets) contributes most to the overall deformation while bearing small actual B−N bond strains. However, B−N bonds in the octagon rings (junctions) are highly strained to convert the imposed vertical strain to the horizontal sheets. This can be inferred from the averaged bond

dx.doi.org/10.1021/jp5044706 | J. Phys. Chem. C 2014, 118, 22730−22738

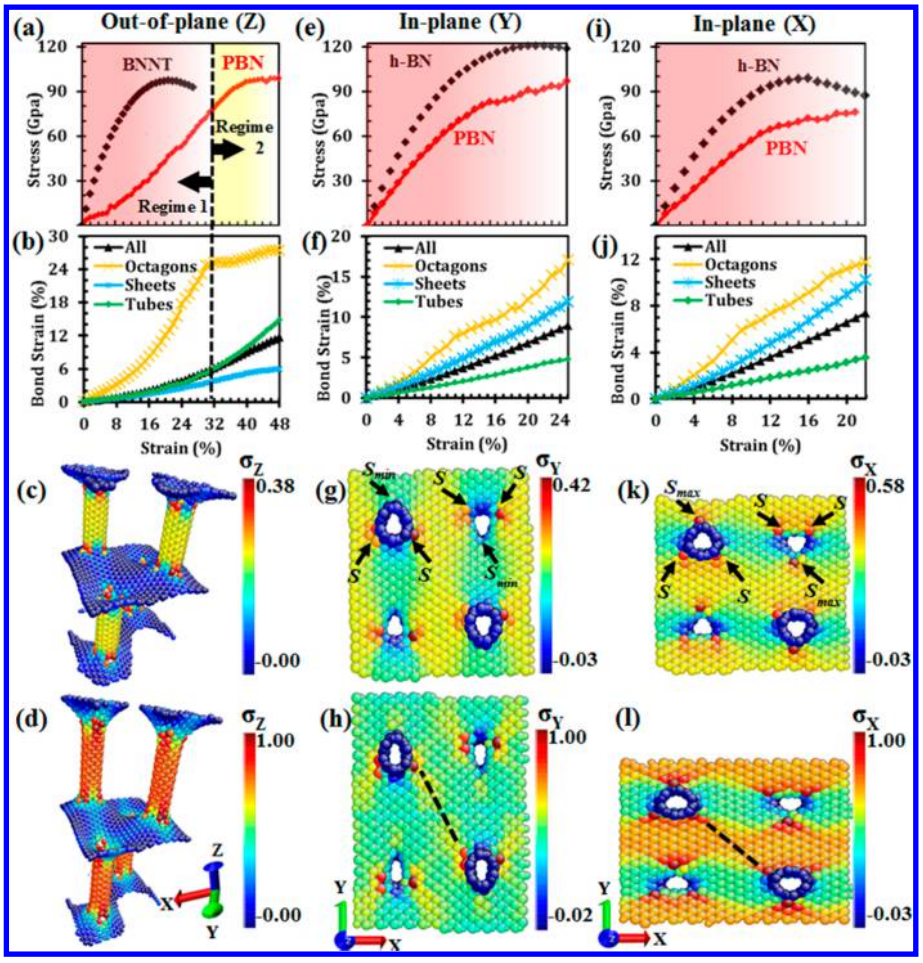

Figure 5. (a) Stress−strain plot of PBN along the *Z* axis exhibits ≈30% higher toughness than pure BNNT while maintaining similar strength. This is enabled by a two-regime deformation mechanism, i.e., geometrical displacement of the sheets, and backbone stretching of the tubes. (b) Average B−N bond strains in the tubes, sheets, and octagon rings as a function of external strain. (c) Stress contour of σ_Z at $\varepsilon_Z \approx 15\%$ (Regime 1). Sheets are minimally stressed. (d) Stress contour of σ_Z at ultimate strain $\varepsilon_Z \approx 48\%$ (Regime 2). Tubes are maximally stressed. (e) Stress−strain plot along the *Y* axis (zigzag). (f) Average B−N bond strains as a function of external strain. (g) Stress contour, σ_Y, at $\varepsilon_Y = 8\%$ depicts stress concentrations at the junctions. One third of the all octagon members are minimally stressed. (h) Stress contour, σ_Y, at ultimate strain $\varepsilon_Y = 26\%$. (i) Stress−strain plot along the *X* axis (armchair). (j) Average B−N bond strains as a function of external strain. (k) Stress contour, σ_X, at $\varepsilon_X = 8\%$. Unlike the zigzag direction, here one-third of the octagons are maximally stressed. (l) Stress contour, σ_X, at ultimate strain $\varepsilon_X = 21\%$. In (h) and (l) the dashed lines show the primary direction of crack propagation that leads to failure. In (c), (d), (g), (h), (k), and (l) the stress values are normalized to the highest stress at ultimate strain in each direction.

strains in Figure 5b and stress concentrations (red dots) in Figure 5c. At $\varepsilon \approx 31\%$ the octagon ring capacities become exhausted, and their bond strains remain almost unchanged. At this point, which is the onset of the second regime (backbone stretching), the majority of the strains starts to be transferred to the BN tubes. In this second regime, the actual B−N bonds in the tubes are significantly stretched until final failure at $\varepsilon_U \approx 48\%$ (Figure 5d).

Together, the first and second deformation regimes provide an out-of-plane toughness (area under the stress−strain curve) of ≈25.9 GPa for PBN, which is ≈30% larger than that of pure BNNT (19.8 GPa). Note that here "toughness" is defined as the amount of energy per volume a material absorbs before failure (representing the work-of-fracture),[47−49] which is different from the classical "fracture toughness" with the unit of $\mathrm{Pa}\sqrt{m}$. The work-of-fracture is the area under the stress−strain curve and is deeply affected by gradual, graceful fracture, whereas the "fracture toughness" does not incorporate this entire process.[49] We stress that it is the first deformation regime that provides the extra ductility and toughness. Interestingly, such a high toughness is not sacrificed by low strength, which is typical in engineered materials.[50,51] This improved balance of strength and toughness along the out-of-plane direction of PBN is a significant result of this paper and is enabled by the synergistic behavior of tubes, junctions, and out-of-plane flexibility of the sheets. A somewhat similar synergistic effect in improving mechanical properties has been experimentally observed for nanocarbons of different dimensionalities.[52]

3.3.2. In-Plane Deformations. Considering in-plane deformation of PBN versus *h*-BN (Figure 5e,i), while the ultimate strains of PBN are close to those of pure *h*-BN, its ultimate stresses and toughnesses are moderately reduced (≈6−8% and ≈29−31%, respectively). This is because of the defects in the sheets, which lead to stress and strain concentrations at the junctions, therefore limiting the total allowable stress (Figure 5f,g,j,k). Indeed, by strain localization around the octagon rings, the cracks initiate at a lower external stress (compared to *h*-BN) and propagate at an inclined angle with respect to the direction of applied load (see dashed lines in Figure 5h,l). This premature stress build-up causes the PBN to have a lower σ_U

dx.doi.org/10.1021/jp5044706 | J. Phys. Chem. C 2014, 118, 22730−22738

along the in-plane directions compared to pure *h*-BN. Furthermore, there is another remarkable difference between the PBN and pure *h*-BN: there is no strain softening phenomenon in PBN along the armchair (X) direction. Strain softening follows the maximum stress until failure is intrinsic to the *h*-BN along its armchair direction and is validated by DFT calculations.[53] In PBN, it appears that the localized nature of strains on the junctions alters the overall in-plane failure mechanism. This will be studied more closely in the future.

Within the in-plane directions of PBN, the ultimate stress, $\sigma_U \approx 106$ GPa, in the zigzag (Y) direction is larger than $\sigma_U \approx 77$ GPa in the armchair (X) direction (cf. Figure 5e,i). This disparity, which in part stems from the bond (zigzag versus armchair) orientations, is also observed in our MD simulation of pure *h*-BN and is verified by DFT calculations on pure *h*-BN.[53] However, there is another mechanism that contributes to this difference in PBN: the octagon rings, which are the hot spots under mechanical loading, undergo different stresses in armchair and zigzag directions. When the PBN is under axial strain in the zigzag direction, one-third of all the octagon rings (symbolized by S_{min} in Figure 5g) is furthest away from the stress concentration points and thus bear minimum stresses (Figure S3, Supporting Information). However, when the PBN is strained along the armchair direction, these same octagon rings (symbolized by S_{max} in Figure 5k) are exactly coincided with the stress concentration points and thus have to sustain maximum stresses (the rest of the octagon rings bear somewhat similar stresses regardless of the direction of applied strain). Therefore, both bond orientation and stress concentrations (arising from asymmetric junctions) in PBN lead to smaller strength capacity along the armchair direction than zigzag direction.

In addition to mechano-mutable functionality of PBN presented above, other potential applications of PBN are for 3D thermal transport, gas storage and separation,[54,55] catalysis,[56,57] and functional porous composites.[58] As an example, compared to the bulk BN or *h*-BN flakes, PBN is a lightweight, porous structure with more than 2250 m^2/g surface area (Table 1). Unlike stacking of *h*-BN, the multiple-fold enhancement in the interlayer distance of PBN (due to integration of nanotubes) allows a significant amount of gases to be physisorbed within the slit pores at low temperature or high pressures. In view of the competing mechanisms between the size of the adsorbate, the surface area, and pore aperture size of the adsorbent,[59] modulating the PD/PL ratio can regulate the aperture and slit sizes of PBN, thus rendering PBN as a potential tunable membrane for separating gas mixtures or as a support for size- and shape-selective catalysis in confined environments.[60]

CONCLUSION

We introduced PBN as a new series of 3D multifunctional BN prototypes by in silico fusing of 1D BNNT and 2D *h*-BN allotropes to moderate the anisotropy of its constituents and to provide new and synergistic functionalities. Unlike the stacking of *h*-BN sheets, which exhibit weak out-of-plane properties, PBN provides substantial improvements in the out-of-plane mechanical properties. In this context, a synergistic geometrical feature is manifest via cooperation of junctions, tubes, and sheets in the 3D architecture. This unique feature can overcome the intrinsic limitations of the 1D and 2D constituents of PBN and impart superior properties including 3D balance of strength and toughness, emergence of negative in-plane Poisson's ratio, and elimination of strain softening in the armchair orientation.

Broadly, our findings lay the foundation for discovering numerous tunable, hybrid 3D BN architectures by fusing low-dimensional BN building blocks including 0D fullerene, 1D nanotubes, and 2D nanosheets. A rich set of hybrid carbon nanostructures have been developed and studied over the past years. However, similar advances for hybrid BN allotropes have thus far remained elusive. To the best of our knowledge, this paper for the first time introduces 3D BN architectures and explores their diverse mechano-mutable properties. Such architectures can complement graphene-based nanoelectronics and can also open up a plethora of opportunities to explore several fascinating nanomaterials such as next-generation 3D semiconductors with adjustable bandgap through doping of other elements into PBN,[16] fabricating porous networks with ultrahigh surface area and tunable aperture/slit size for gas adsorption and catalysis, and creating 3D thermal transport devices with implications in nanoscale calorimeters, microelectronic processes, and macroscopic refrigerators.[61]

ASSOCIATED CONTENT

Supporting Information

Comparison of DFT versus MD results on the stress−strain response, elastic constant tensors of PBN_I to PBN_IV, effective versus equivalent elastic moduli of PBN, relation between the location of octagon rings and stress concentration points, and three movies of the in-plane (armchair and zigzag) and out-of-plane deformations of PBN_IV. All atomic structures of the PBN prototypes are in XYZ format, and scripts used in this study are available from the corresponding author upon request. This material is available free of charge via the Internet at http://pubs.acs.org.

AUTHOR INFORMATION

Corresponding Author

*E-mail: rouzbeh@rice.edu.

Author Contributions

R.S. designed the research; N.S and R.S performed the computational and experimental research; N.S. analyzed the data; and N.S. and R.S. wrote the paper.

Notes

The authors declare no competing financial interest.

ACKNOWLEDGMENTS

This project was supported partially by Rice University and partially by the National Science Foundation grant number CMMI-1235522. The supercomputer machines utilized in this work were supported in part by NIH award NCRR S10RR02950 and an IBM Shared University Research (SUR) Award in partnership with CISCO, Qlogic and Adaptive Computing, and in part by the Data Analysis and Visualization Cyber infrastructure funded by NSF under grant OCI-0959097.

REFERENCES

(1) Chopra, N. G.; Luyken, R. J.; Cherrey, K.; Crespi, V. H.; Cohen, M. L.; Louie, S. G.; Zettl, A. Boron Nitride Nanotubes. *Science* **1995**, *269*, 966−967.

(2) Golberg, D.; Bando, Y.; Tang, C. C.; Zhi, C. Y. Boron Nitride Nanotubes. *Adv. Mater.* **2007**, *19*, 2413−2432.

(3) Harris, P. J. F. *Carbon Nanotubes and Related Structures: New Materials for the Twenty-first Century*; Cambridge University Press: New York, 2001.

(4) Novoselov, K. S.; Geim, A. K.; Morozov, S. V.; Jiang, D.; Zhang, Y.; Dubonos, S. V.; Grigorieva, I. V.; Firsov, A. A. Electric Field Effect in Atomically Thin Carbon Films. *Science* **2004**, *306*, 666−669.
(5) Chang, C. W.; Okawa, D.; Majumdar, A.; Zettl, A. Solid-State Thermal Rectifier. *Science* **2006**, *314*, 1121−1124.
(6) Chopra, N. G.; Zettl, A. Measurement of the Elastic Modulus of a Multi-Wall Boron Nitride Nanotube. *Solid State Commun.* **1998**, *105*, 297−300.
(7) Rubio, A.; Corkill, J. L.; Cohen, M. Theory of Graphitic Boron Nitride Nanotubes. *Phys. Rev. B* **1994**, *49*, 5081−5084.
(8) Golberg, D.; Bando, Y.; Kurashima, K.; Sato, T. Synthesis and Characterization of Ropes Made of BN Multiwalled Nanotubes. *Scr. Mater.* **2001**, *44*, 1561−1565.
(9) Nakhmanson, S. M.; Calzolari, A.; Meunier, V.; Bernholc, J.; Nardelli, M. B. Spontaneous Polarization and Piezoelectricity in Boron Nitride Nanotubes. *Phys. Rev. B* **2003**, *67*, 235406.
(10) Park, J.; Prakash, V. Thermal Transport in 3D Pillared SWCNT−Graphene Nanostructures. *J. Mater. Res.* **2013**, *28*, 940−951.
(11) Chang, C. W.; Fennimore, A. M.; Afanasiev, A.; Okawa, D.; Ikuno, T.; Garcia, H.; Li, D.; Majumdar, A.; Zettl, A. Isotope Effect on the Thermal Conductivity of Boron Nitride Nanotubes. *Phys. Rev. Lett.* **2006**, *97*, 085901.
(12) Lee, J.; Kim, H.; Kahng, S. J.; Kim, G.; Son, Y. W.; Ihm, J.; Kato, H.; Wang, Z. W.; Okazaki, T.; Shinohara, H.; et al. Bandgap Modulation of Carbon Nanotubes by Encapsulated Metallofullerenes. *Nature* **2002**, *415*, 1005−1008.
(13) Nasibulin, A. G.; Pikhitsa, P. V.; Jiang, H.; Brown, D. P.; Krasheninnikov, A. V.; Anisimov, A. S.; Queipo, P.; Moisala, A.; Gonzalez, D.; Lientschnig, G.; et al. A Novel Hybrid Carbon Material. *Nat. Nanotechnol.* **2007**, *2*, 156−161.
(14) Wu, X.; Zeng, X. C. Periodic Graphene Nanobuds. *Nano Lett.* **2009**, *9*, 250−256.
(15) Dimitrakakis, G. K.; Tylianakis, E.; Froudakis, G. E. Pillared Graphene: A New 3-D Network Nanostructure for Enhanced Hydrogen Storage. *Nano Lett.* **2008**, *8*, 3166−3170.
(16) Song, L.; Liu, Z.; Reddy, A. L. M.; Narayanan, N. T.; Taha-Tijerina, J.; Peng, J.; Gao, G.; Lou, J.; Vajtai, R.; Ajayan, P. M. Binary and Ternary Atomic Layers Built from Carbon, Boron, and Nitrogen. *Adv. Mater.* **2012**, *24*, 4878−4895.
(17) Wang, W.; Bando, Y.; Zhi, C.; Fu, W.; Wang, E.; Golberg, D. Aqueous Noncovalent Functionalization and Controlled Near-Surface Carbon Doping of Multiwalled Boron Nitride Nanotubes. *J. Am. Chem. Soc.* **2008**, *130*, 8144−8145.
(18) Xu, Z.; Lu, W.; Wang, W.; Gu, C.; Liu, K.; Bai, X.; Wang, E.; Dai, H. Converting Metallic Single-Walled Carbon Nanotubes into Semiconductors by Boron/Nitrogen Co-Doping. *Adv. Mater.* **2008**, *20*, 3615−3619.
(19) Kumar, N.; Raidongia, K.; Mishra, A. K.; Waghmare, U. V.; Sundaresan, A.; Rao, C. N. R. Synthetic Approaches to Borocarbonitrides, BCxN (x=1−2). *J. Solid State Chem.* **2011**, *184*, 2902−2908.
(20) Britnell, L.; Gorbachev, R. V.; Jalil, R.; Belle, B. D.; Schedin, F.; Mishchenko, A.; Georgiou, T.; Katsnelson, M. I.; Eaves, L.; Morozov, S. V.; et al. Field-Effect Tunneling Transistor Based on Vertical Graphene Heterostructures. *Science* **2012**, *335*, 947−950.
(21) Yan, Z.; Peng, Z.; Sun, Z.; Yao, J.; Zhu, Y.; Liu, Z.; Ajayan, P. M.; Tour, J. M. Growth of Bilayer Graphene on Insulating Substrates. *ACS Nano* **2011**, *5*, 8187−8192.
(22) Gao, G.; Gao, W.; Cannuccia, E.; Taha-Tijerina, J.; Balicas, L.; Mathkar, A.; Narayanan, T. N.; Liu, Z.; Gupta, B. K.; Peng, J.; et al. Artificially Stacked Atomic Layers: Toward New van der Waals Solids. *Nano Lett.* **2012**, *12*, 3518−3525.
(23) Golberg, D.; Bando, Y.; Huang, Y.; Terao, T.; Mitome, M.; Tang, C.; Zhi, C. Boron Nitride Nanotubes and Nanosheets. *ACS Nano* **2010**, *4*, 2979−2993.
(24) Plimpton, S. Fast Parallel Algorithms for Short-Range Molecular Dynamics. *J. Comput. Phys.* **1995**, *117*, 1−19.
(25) Albe, K.; Möller, W. Modelling of Boron Nitride: Atomic Scale Simulations on Thin Film Growth. *Comput. Mater. Sci.* **1998**, *10*, 111−115.
(26) Sekkal, W.; Bouhafs, B.; Aourag, H.; Certier, M. Molecular-Dynamics Simulation of Structural and Thermodynamic Properties of Boron Nitride. *J. Phys.: Condens. Matter* **1998**, *10*, 4975−4984.
(27) Won Ha, M.; Ho Jung, H. Molecular-Dynamics Simulation of Structure and Thermal Behaviour of Boron Nitride Nanotubes. *Nanotechnology* **2004**, *15*, 431−434.
(28) Vaccarini, L.; Goze, C.; Henrard, L.; Hernández, E.; Bernier, P.; Rubio, A. Mechanical and Electronic Properties of Carbon and Boron−Nitride Nanotubes. *Carbon* **2000**, *38*, 1681−1690.
(29) Verma, V.; V. K, J.; Dharamvir, K. Elastic Moduli of a Boron Nitride Nanotube. *Nanotechnology* **2007**, *18*, 435711.
(30) Nose, S. A Unified Formulation of the Constant Temperature Molecular Dynamics Methods. *J. Chem. Phys.* **1984**, *81*, 511−519.
(31) Hoover, W. G. Canonical Dynamics: Equilibrium Phase-Space Distributions. *Phys. Rev. A* **1985**, *31*, 1695−1697.
(32) Humphrey, W.; Dalke, A.; Schulten, K. VMD: Visual Molecular Dynamics. *J. Mol. Graphics* **1996**, *14*, 33−38.
(33) Li, J. AtomEye: an Efficient Atomistic Configuration Viewer. *Modell. Simul. Mater. Sci. Eng.* **2003**, *11*, 173−177.
(34) Okada, S.; Saito, S.; Oshiyama, A. Energetics and Electronic Structures of Encapsulated C60 in a Carbon Nanotube. *Phys. Rev. Lett.* **2001**, *86*, 3835−3838.
(35) Shahsavari, R.; Buehler, M. J.; Pellenq, R. J. M.; Ulm, F.-J. First-Principles Study of Elastic Constants and Interlayer Interactions of Complex Hydrated Oxides: Case Study of Tobermorite and Jennite. *J. Am. Ceram. Soc.* **2009**, *92*, 2323−2330.
(36) Nye, J. F. *Physical Properties of Crystals*; Oxford University Press: Oxford, England, 1957.
(37) Parr, R. G.; Yang, W. *Density-Functional Theory of Atoms and Molecules*; Oxford University Press: USA, 1994.
(38) Hornbaker, D. J.; Kahng, S.-J.; Misra, S.; Smith, B. W.; Johnson, A. T.; Mele, E. J.; Luzzi, D. E.; Yazdani, A. Mapping the One-Dimensional Electronic States of Nanotube Peapod Structures. *Science* **2002**, *295*, 828−831.
(39) Vanderbilt, D. Soft Self-Consistent Pseudopotentials in a Generalized Eigenvalue Formalism. *Phys. Rev. B* **1990**, *41*, 7892−7895.
(40) Giannozzi, P.; Baroni, S.; Bonini, N.; Calandra, M.; Car, R.; Cavazzoni, C.; Ceresoli, D.; Chiarotti, G. L.; Cococcioni, M.; Dabo, I.; et al. QUANTUM ESPRESSO: A Modular and Open-Source Software Project for Quantum Simulations of Materials. *J. Phys.: Condens. Matter* **2009**, *21*, 395502.
(41) Baowan, D.; Cox, B. J.; Hill, J. M. Two Least Squares Analyses of Bond Lengths and Bond Angles for the Joining of Carbon Nanotubes to Graphenes. *Carbon* **2007**, *45*, 2972−2980.
(42) Cromwell, P. R. *Polyhedra*; Cambridge University Press: New York, 1997.
(43) Baowan, D.; Cox, B. J.; Hill, J. M. Junctions Between a Boron Nitride Nanotube and a Boron Nitride Sheet. *Nanotechnology* **2008**, *19*, 075704.
(44) Boldrin, L.; Scarpa, F.; Chowdhury, R.; Adhikari, S. Effective Mechanical Properties of Hexagonal Boron Nitride Nanosheets. *Nanotechnology* **2011**, *22*, 505702.
(45) Grima, J. N.; Jackson, R.; Alderson, A.; Evans, K. E. Do Zeolites Have Negative Poisson's Ratios? *Adv. Mater.* **2000**, *12*, 1912−1918.
(46) Yang, W.; Li, Z.-M.; Shi, W.; Xie, B.-H.; Yang, M.-B. Review on Auxetic Materials. *J. Mater. Sci.* **2004**, *39*, 3269−3279.
(47) Meyers, M. A.; McKittrick, J.; Chen, P.-Y. Structural Biological Materials: Critical Mechanics-Materials Connections. *Science* **2013**, *339*, 773−779.
(48) Wegst, U. G. K.; Ashby, M. F. The Mechanical Efficiency of Natural Materials. *Philos. Mag.* **2004**, *84*, 2167−2186.
(49) Meyers, M. A.; Chen, P.-Y.; Lin, A. Y.-M.; Seki, Y. Biological Materials: Structure and Mechanical Properties. *Prog. Mater. Sci.* **2008**, *53*, 1−206.
(50) Ritchie, R. O. The Conflicts Between Strength and Toughness. *Nat. Mater.* **2011**, *10*, 817−822.
(51) Sakhavand, N.; Muthuramalingam, P.; Shahsavari, R. Toughness Governs the Rupture of the Interfacial H-Bond Assemblies at a Critical Length Scale in Hybrid Materials. *Langmuir* **2013**, *29*, 8154−8163.

(52) Prasad, K. E.; Das, B.; Maitra, U.; Ramamurty, U.; Rao, C. N. R. Extraordinary Synergy in the Mechanical Properties of Polymer Matrix Composites Reinforced with 2 Nanocarbons. *Proc. Natl. Acad. Sci. U.S.A.* **2009**, *106*, 13186−13189.
(53) Peng, Q.; Ji, W.; De, S. Mechanical Properties of the Hexagonal Boron Nitride Monolayer: Ab Initio Study. *Comput. Mater. Sci.* **2012**, *56*, 11−17.
(54) Weng, Q.; Wang, X.; Zhi, C.; Bando, Y.; Golberg, D. Boron Nitride Porous Microbelts for Hydrogen Storage. *ACS Nano* **2013**, *7*, 1558−1565.
(55) Nag, A.; Raidongia, K.; Hembram, K. P. S. S.; Datta, R.; Waghmare, U. V.; Rao, C. N. R. Graphene Analogues of BN: Novel Synthesis and Properties. *ACS Nano* **2010**, *4*, 1539−1544.
(56) Meyer, N.; Bekaert, K.; Pirson, D.; Devillers, M.; Hermans, S. Boron Nitride as an Alternative Support of Pd Catalysts for the Selective Oxidation of Lactose. *Catal. Commun.* **2012**, *29*, 170−174.
(57) Wang, L.; Sun, C.; Xu, L.; Qian, Y. Convenient Synthesis and Applications of Gram Scale Boron Nitride Nanosheets. *Catal. Sci. Technol.* **2011**, *1*, 1119−1123.
(58) Rafiee, M. A.; Narayanan, T. N.; Hashim, D. P.; Sakhavand, N.; Shahsavari, R.; Vajtai, R.; Ajayan, P. M. Hexagonal Boron Nitride and Graphite Oxide Reinforced Multifunctional Porous Cement Composites. *Adv. Funct. Mater.* **2013**, *23*, 5624−5630.
(59) Prakash, M.; Sakhavand, N.; Shahsavari, R. H2, N2, and CH4 Gas Adsorption in Zeolitic Imidazolate Framework-95 and −100: Ab Initio Based Grand Canonical Monte Carlo Simulations. *J. Phys. Chem. C* **2013**, *117*, 24407−24416.
(60) Lu, G.; Li, S.; Guo, Z.; Farha, O. K.; Hauser, B. G.; Qi, X.; Wang, Y.; Wang, X.; Han, S.; Liu, X.; et al. Imparting Functionality to a Metal−Organic Framework Material by Controlled Nanoparticle Encapsulation. *Nat. Chem.* **2012**, *4*, 310−316.
(61) Pakdel, A.; Zhi, C.; Bando, Y.; Golberg, D. Low-Dimensional Boron Nitride Nanomaterials. *Mater. Today* **2012**, *15*, 256−265.